

Experimental Analysis of Dragonfly-Inspired Airfoils at a Reynolds Number of 4000

Final Report

Marko Danial, Andy Glover, Joshua Liao, Alex Suvorov

UNIVERSITY OF SOUTHERN CALIFORNIA

DEPARTMENT OF AEROSPACE AND MECHANICAL ENGINEERING

AME-441A: SENIOR PROJECTS LABORATORY – Group #24

Abstract

Dragonfly wings have a characteristic “corrugated” shape that has been speculated to be the cause of high lift and high maneuverability [2]. An experimental study was conducted to determine the lift performance of dragonfly-inspired airfoils in the small water channel in the RRB small water channel at USC. The experimental design was guided by a numerical study by Tang et al which showed an improvement of lift coefficient, C_L , over various angles of attack, α [4]. Three airfoils were chosen: a control NACA 2410, a simplification of the dragonfly airfoil from the numerical study [4], and an experimental concept of increasing the number of corrugations in the wing. The airfoils were held by a vertically suspended cantilever beam and the lift force was measured by the deflection of the beam in the direction perpendicular to the water flow. The C_L data for the three airfoils showed overlapping uncertainty values and no definitive statements of airfoil performance can be made. However, the mean values are suggestive of similar trends between the dragonfly airfoil as predicted by Tang et al. [4]: a average mean C_L value increase of 27% between $\alpha = 0^\circ$ and $\alpha = 6^\circ$ was found between the dragonfly airfoil and the control. Also, the flow over the wing was visualized and the predicted vorticity in the upper corrugations by the study [4] was experimentally reproduced in the dragonfly airfoil.

Table of Contents

1. Introduction	3
1.1 Generating Lift.....	3
1.2 Wing Shape: Effects and Nomenclature.....	3
1.2.1 Effects.....	3
1.2.2 Nomenclature	3
1.3 Taking Inspiration from Nature	3
1.3.1 Design Optimization Techniques.....	3
1.3.2 A Numerical CFD Study of Dragonfly Airfoils.....	4
1.4 Comments on Drag.....	6
1.5 Quantifying and Manipulating Turbulence	6
2. Experimental Setup and Procedure	7
2.1 Airfoil Design	7
2.2 Cantilever Beam Design	8
2.3 AoA Connector Design.....	9
2.4 Experimental Setup	9
2.5 Procedure	11
2.5.1 Calibration of the Strain Gauges	11
2.5.2 Water Channel Testing	12
3. Results	12
3.1 Calibration Results.....	12
3.2 Lift Coefficient (CL) vs. Angle of Attack (α).....	14
3.3 Flow Visualization.....	14
4. Discussion	15
4.1 Stall Angle Challenges	15
4.2 Performance Comparison of the Airfoil Designs	16
4.3 Sources of Uncertainty	17
4.4 Capturing the Vorticity	18
4.5 Project Cost Breakdown	18
5. Conclusion	19
5.1 Summary	19
5.2 Recommendations	19
6. References	20
7. Appendices	21
7.1 Appendix A: Budget Analysis.....	21
7.2 Appendix B: Engineering CAD Drawings.....	22

1. Introduction

1.1 Generating Lift

Wings that react against air can generate an upward lift force by manipulating three key geometric parameters: the cross-sectional shape of the wing itself, the incident angle in which that wing collides with the oncoming flow of air, and the quantifiable turbulence of that flow. This experiment aims to evaluate the lifting abilities for variations of airfoil shape, over a range of incidence angles—designated the angle of attack (AoA or α)—while nullifying the effects of turbulence (defined in Section 1.5) by keeping it at a specifically chosen constant in all cases.

1.2 Wing Shape: Effects and Nomenclature

1.2.1 Effects

Wings utilize a specific geometry that redirects a flow of oncoming air to create a static pressure differential (acting normal) between the top and bottom surfaces. When there is less force acting on the top surface of the wing than the bottom, the resultant aerodynamic force acts in the upward direction, called *lift*. Since aerodynamic forces are scaled by the area of the wing and the dynamic pressure of the oncoming flow, comparing the lifting abilities of a wing's shape requires non-dimensional quantities—where area and dynamic pressure have been factored out. The following are the non-dimensional expressions of pressure, C_P , and lift, C_L ,

$$C_P = \frac{P}{\frac{1}{2}\rho U_0^2} \quad \& \quad C_L = \frac{F_L}{\frac{1}{2}\rho U_0^2} \quad 1$$

where the absolute forces of static pressure, P , and Lift, F_L , have been normalized by the wing area, S , and the dynamic pressure components of flow density, ρ , and flow speed, U_0 .

1.2.2 Nomenclature

Shape in the context of this experiment is classified using the term airfoil. An airfoil is a two-dimensional (2D) cross sectional area of a wing that is oriented perpendicularly to the oncoming flow and therefore has no finite wingspan [1]. The airfoil is defined by its chord length, c , the dimension parallel to the flow, and the thickness, t , the dimension parallel to lift. In a wind tunnel or water channel test section, a physical wing can be approximated as an “infinite” 2D wing if the cross-sectional area remains constant over the entire wing’s span and there are little to no wingtip affects [1]. This, then leads to the task of finding new airfoil shapes that might be of interest to study against what are currently used in the aviation industry.

1.3 Taking Inspiration from Nature

1.3.1 Design Optimization Techniques

The lift of an airfoil can be found as the pressure differential integrated over the entire chord length [1]. Therefore, the way to optimize the shape of an airfoil is to apply flow equations where the static pressure of the flow can be calculated at each point along the chord. The next step would be manipulating airfoil geometry for maximum C_P at every chord location. As Anderson points out, there is no closed form solution to which an inputted flow field and airfoil geometry

output a C_p distribution [1]. Therefore, the amount of lift an airfoil generates cannot currently be optimized analytically [1]. Thus, a system of acquiring the lift characteristics of an airfoil is needed through iterative and experimental methods [1]. A place of experimental interest is nature because, as Deubel et al. points out, evolution has been an exercise in experimental optimization for millions of years [2]. Deubel et al. specifically shows interest in the flying abilities of the dragonfly, given their high-maneuverability and ability to achieve lift within a couple of strokes—with an emphasis on their airfoil shape being a potential reason for this [2]. For this experiment, the dragonfly airfoil shape is classified as *corrugated*—characterized by a series of peaks and valleys along the chord. **Fig. 1** shows a diagram by Deubel et al. demonstrating this shape and its predicted aerodynamic effects [2].

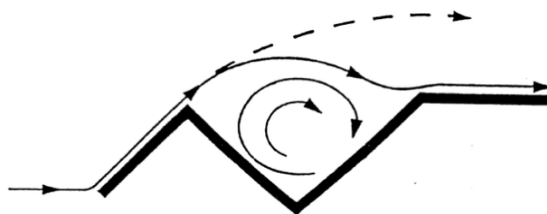


Figure 1. A depiction of a corrugated wing from Deubel et al. [2]. Image mirrored from source to match flow direction convention in this experiment.

The shape in **Fig. 1** is one section of corrugation meant to portray the aerodynamic effects of the peaks and valleys. A finalized representation of the dragonfly airfoil is to be shown in the following sections. The left peak in **Fig. 1** is shown tripping the streamline present in the boundary layer by adding clockwise vorticity [2]. This tripped flow then settles within the valley formed by the left and right peaks, creating a fully attached segment of lower-than-freestream static pressure [2]. The prediction is that the low pressure created in these valleys will increase the C_p differential between top and bottom surface compared to a conventional airfoil of similar thickness [2]. For this experiment, a conventional airfoil is classified as one having the characteristic “teardrop” shape as seen in the NACA series of airfoils [3]. Therefore, before comparing the lifting performance of these alternative airfoils against conventional ones, it is worth finding numerical predictions to guide the design of the experiment.

1.3.2 A Numerical CFD Study of Dragonfly Airfoils

A study by Tang et al. conducted a 2D numerical simulation of dragonfly airfoils, with the same characteristic corrugations as seen in **Fig. 1** [4]. The numerical method applied by Tang et al. utilized the continuity equation (conservation of mass) and the Arbitrary Lagrangian-Eulerian simplified version of the Navier-Stokes equations for a simplified dragonfly airfoil [4]. This system of equations was solved at a Reynolds number of 4000 (see Section 1.4) [4].

Their resulting C_P distribution is shown in **Fig. 2** with the color bar representing the C_P deviation from the freestream static pressure [4].

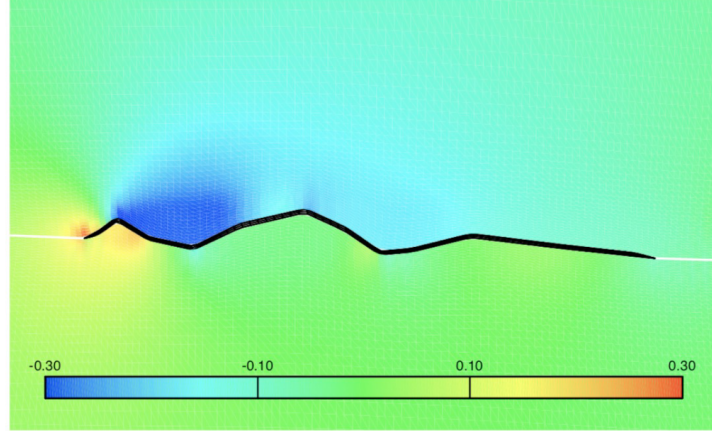


Figure 2. Pressure distribution of corrugated airfoil of $\alpha = 2^\circ$, from numerical simulation by Tang et al. [4].

Tang et al. shows how the corrugations are implemented in the airfoil [4]. As seen in **Fig. 2**, their numerical study captured the lower pressure in the two upper valleys [4]. Furthermore, Tang et al. also conducted a numerical simulation tracking the laminar streamlines as they traverse the airfoil[4], shown in **Fig. 3**.

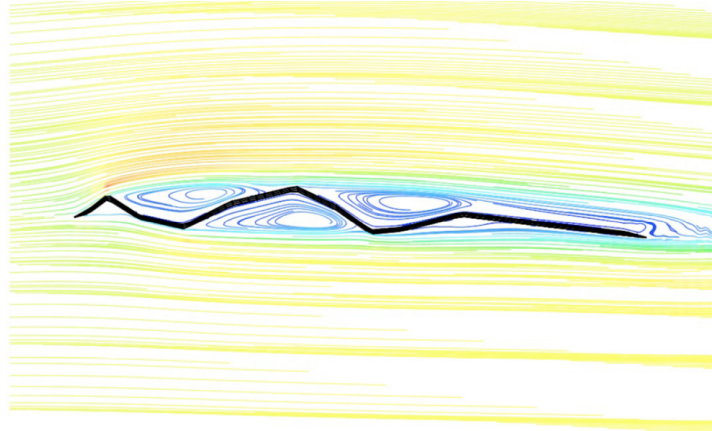


Figure 3. Streamlines around corrugated airfoil of $\alpha = 2^\circ$, from numerical simulation by Tang et al [4].

Tang et al. (as shown in **Fig. 3**) has captured the vorticity in the valleys of the corrugations [4]. It is worth noting that the streamlines in the case of the lower surface also show vorticity. This suggests the significance of the angle of attack, since while the bottom may show vorticity, it directly faces the oncoming dynamic pressure and therefore has higher static pressure as seen in **Fig. 2**. Furthermore, Tang et al. uses the streamline visualization in **Fig. 3** to determine that a NACA 2408 is a conventional airfoil of appropriate comparison, since the profile flow of the dragonfly wing (shown as the boundary between yellow and turquoise) roughly traces its perimeter [4].

Shown in **Fig. 4** is the comparison of C_L at various angles of attack, α from Tang et al. [4].

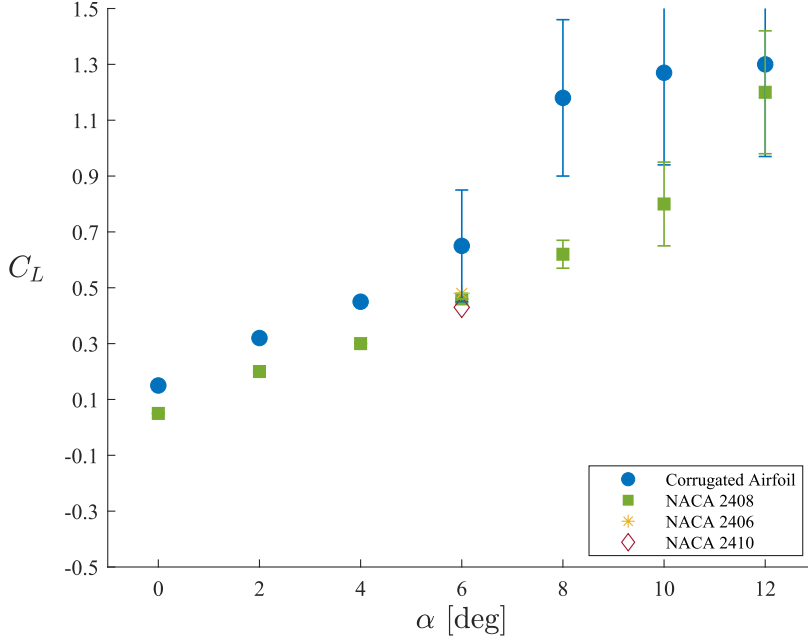


Figure 4. Replicated numerical data from Tang et al [4] showing an improvement in C_L vs. α for the dragonfly inspired wing. Some error bars cut off by scale for clarity.

1.4 Comments on Drag

Since lift-to-drag ratios for airfoils are on the order of magnitude of 10 [1], expected drag forces will be harder to capture with experimental equipment. For reasons that will be mathematically apparent in Section 2, the scope of the experiment is restricted to lift (and thus maneuverability) performance.

1.5 Quantifying and Manipulating Turbulence

As pointed out in Section 1.3.2, the Reynolds number was purposely held at $Re = 4000$ in the study by Tang et al. [4]. Reynolds number is the non-dimensional quantification of the relative turbulence a flow experiences as it traverses around a surface [1]. It measures the inertial forces of the flow as a proportion of its viscous forces, shown in Eq. 2.

$$Re = \frac{\rho U_0 c}{\mu} \quad 2$$

where ρ is the density of the fluid, U_0 is the flow velocity, the characteristic length, c , is the airfoil chord, and μ is the dynamic viscosity of the fluid [1]. A Reynolds number of 4000 is classified as laminar flow, the type which may be experienced by dragonflies and miniature unmanned aerial vehicles (UAVs), and therefore worthy of study for emerging drone applications [4]. Laminar flow is one where the relative viscous forces dominate, and therefore, the flow can be depicted as a set of parallel (non-mixing, no vorticity) streamlines, as seen in the freestream flow in the lefthand side of **Fig. 3**. Finally, as was pointed out by Anderson, the number of assumptions a

numerical study must make is motivation for physical experimental testing in actual flows [1]. Therefore, the purpose of this project is to best apply the numerical study by Tang et al. to a physical evaluation of lift in a water channel.

2. Experimental Setup and Procedure

2.1 Airfoil Design

The three airfoils used in this study were designed to evaluate the aerodynamic performance of dragonfly-inspired corrugated airfoils at a Reynolds number of 4000. These airfoils include a smooth NACA 2410 airfoil, an intermediate corrugated airfoil, and an extreme corrugated airfoil, all designed with a chord length of 10 cm and a span of 20 cm. The intermediate and extreme corrugated airfoils were based on the NACA 2410 profile and maintained a consistent thickness of 3 mm, matching the smooth airfoil's profile for comparisons. As shown in **Fig. 5**, the CAD models illustrate the distinct surface geometries of the airfoils, highlighting their differences in surface texture and corrugation.

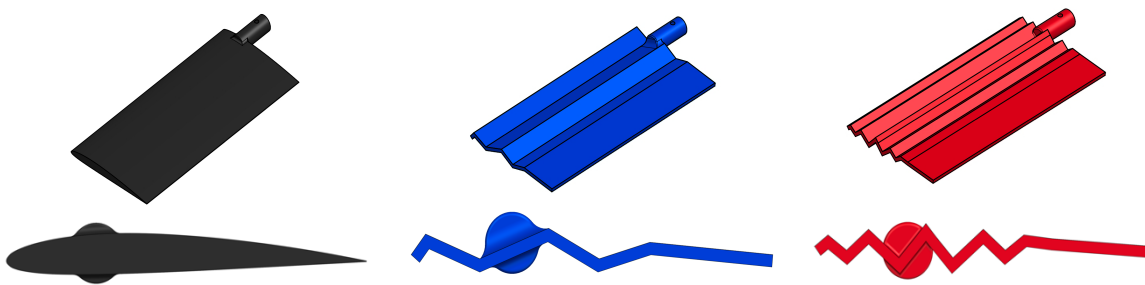


Figure 5. CAD models of the smooth (black), intermediate corrugated (blue), and extreme corrugated (red) airfoils.

A thickness of 3 mm was chosen due to the 3D printing limitations and to add structural integrity for the intermediate and extreme airfoils. This is a deviation from the study by Tang et al., which used a 1% of chord length for the thickness [4]. To compensate for this, the thickness-to-chord ratio of the conventional airfoil used for this experiment was moved from 8% to 10%, more closely matching the outline of a NACA 2410 as opposed to a NACA 2408.

The smooth airfoil, represented in **black**, served as the control and followed the standard NACA 2410 profile; it provided the baseline performance data to compare against the bio-inspired corrugated designs.

The intermediate corrugated airfoil, shown in **blue**, was designed to replicate the dimensions and corrugation patterns described in the study by Tang et al. [4], which can also be referred to in **Fig. 2** and **Fig. 3**. This design featured moderate pleating along its chord length, inspired by dragonfly wings.

The extreme corrugated airfoil, displayed in **red**, was developed by compressing the pleats of the intermediate design into a more densely packed pattern over the same proportion of chord length. This experimental design aimed to explore the aerodynamic limits of corrugation, seeking

to maximize vortex generation and pressure reduction. For detailed engineering drawings of the CAD models of the three airfoils, refer to **Appendix B**.

2.2 Cantilever Beam Design

The choice of water was done to get the highest forces due to the approximately 1000 times higher density of water compared to air. The action of a lifting airfoil then deflects a vertically suspended cantilever beam, whose deflection can be equated as a lift force (see **Eq. 1** below). The cantilever beam was manufactured from 2-inch x 24-inch Aluminum 6061 sheets from McMaster and Carr. To generate as much deflection as possible, the lowest thickness available of 1.016 mm (0.04 in) was chosen. The maximum expected lift force for the study was calculated using the maximum lift coefficient recorded from the study by Tang et. Al of $C_L = 1.25$ at $\alpha = 12^\circ$. Using this max lift coefficient, the maximum lift force could be calculated by using **Eq. 3**,

$$C_L = \frac{F_L}{\frac{1}{2} \rho U_0^2 S} \quad 3$$

where F_L represents lift force, ρ is density of the medium, U_0 is flow speed, and S is wing area. With **Eq. 3**, a maximum lift force of 20 mN was derived. The maximum deflection could then also be derived using **Eq. 4**,

$$\delta = \frac{F_L L^3}{3EI} \quad 4$$

where L is the length of the beam, E is the elastic modulus for Al 6061, and I is the area moment of inertia of the beam's cross section perpendicular to its longitudinal direction.

The maximum deflection δ was calculated to be 9 cm. With these expected values, two *Omega SGD-7/350-LY13* precision strain gauges were glued to the top of the cantilever beam to measure voltages generated by its deflection from the aerodynamic forces coming off the airfoils. A CAD image of the cantilever beam can be seen in **Fig. 6**.

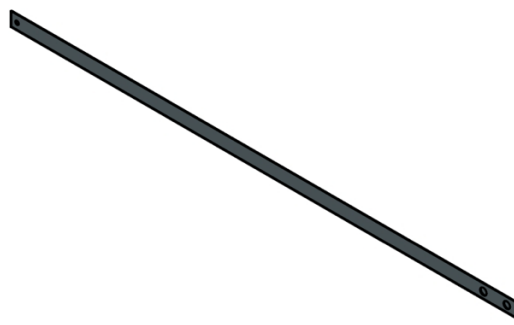


Figure 6. CAD model of the cantilever beam used for measuring deflection.

By setting the strain gauges at the top of the beam, the deflections at the bottom of the beam—connected with the airfoil—could be recorded. For a detailed engineering drawing of the CAD model for the cantilever beam, refer to **Appendix B**.

2.3 AoA Connector Design

The design of the angle of attack (AoA or α) connector was key in allowing simple to manufacture but precise adjustments of the airfoil's orientation during testing. The AoA connector served as the interface between the airfoil and the cantilever beam, allowing for secure mounting and controlled manipulation of the airfoil's angle relative to the flow. The connectors were 3D printed with ABS filament for its strength, stability, and precision.

The connector featured two key ends: one with a slit for inserting and securing the cantilever beam using 8-32 x 1-inch screws, and the other designed to attach to the cylindrical extrusion on the airfoil. The cylindrical attachment was secured with 10-36 x 1-inch screws, providing a sturdy and adjustable connection. The depth of the slit was calibrated to ensure a snug fit, minimizing undesired movement during testing. The connector piece model for an AoA of 3° is displayed in **Fig. 7**.

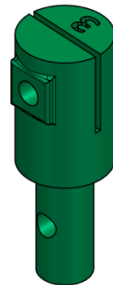


Figure 7. CAD model of the connector piece designed to join the cantilever beam and airfoil.

Connector pieces were 3D printed to cover a range of angles from -3° to 17° . This design allowed for testing across multiple configurations. The choice of 17° was selected as it provided a 5° buffer above the maximum AoA tested in the study by Tang et al. [4], with the intent that the stall angle could still be captured if it occurred beyond their tested range. For a detailed engineering drawing of the CAD model for the AoA connector piece, refer to **Appendix B**.

2.4 Experimental Setup

The experimental setup design first started with the aluminum t-slot apparatus that would hold the cantilever beam, AoA connector piece, and airfoil above the water channel. The goal was to have as much of the airfoil submerged in water as possible (a couple of millimeters above the water channel bottom surface). The components that made up the aluminum t-slot apparatus include: 1.5-inch x 1.5-inch aluminum smooth rail texture T-slot rails, silver 1.5-inch x 1.5-inch corner brackets, silver 1" extended corner brackets, 18-8 stainless steel button head hex drive screws, M2 x 0.4 mm fully threaded screws, 10-32 x $\frac{3}{4}$ flathead screws, size #10 hex nuts, steel offset-barrel narrow-base weld nuts, and 1" single nuts with center holes. The parts list that specifies the quantities and exact composition of the apparatus can be viewed in **Appendix B**.

An exploded view CAD drawing of the Aluminum T-slot apparatus can also be seen in **Fig. 8.**

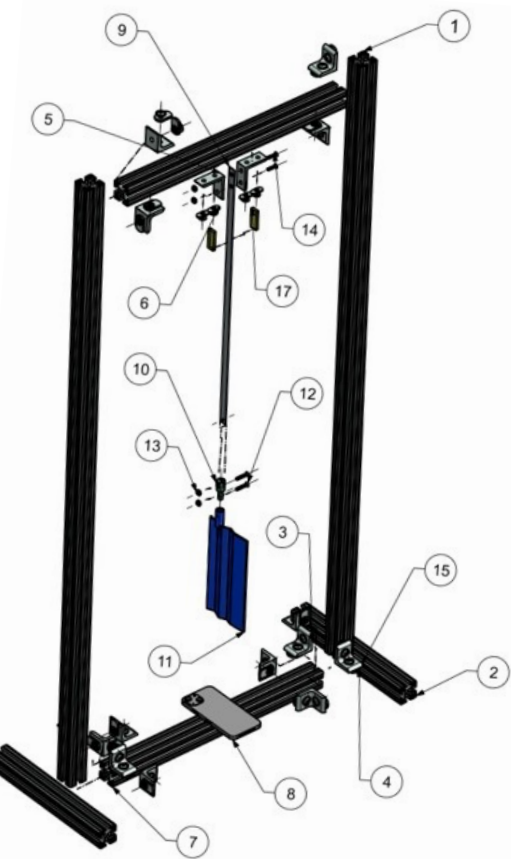


Figure 8. CAD model of the Aluminum T-slot apparatus used to hold the airfoil a few millimeters above the water channel bottom surface (numbered list in **Appendix B**).

The height of the two vertical t-slots on each side were precisely chosen to be 129 cm to ensure that the airfoil was held a few millimeters above the bottom surface of the water channel. The distance between the two t-slots was 49 cm , and that was chosen as the length of the two t-slots going across to connect the two vertical t-slots. The legs on each side were also chosen to be 29 cm to fit the constraints of the water channel table and provide as much stability as possible for the overall setup.

A depiction of the aluminum t-slot apparatus and water channel together can be seen in Fig. 9.

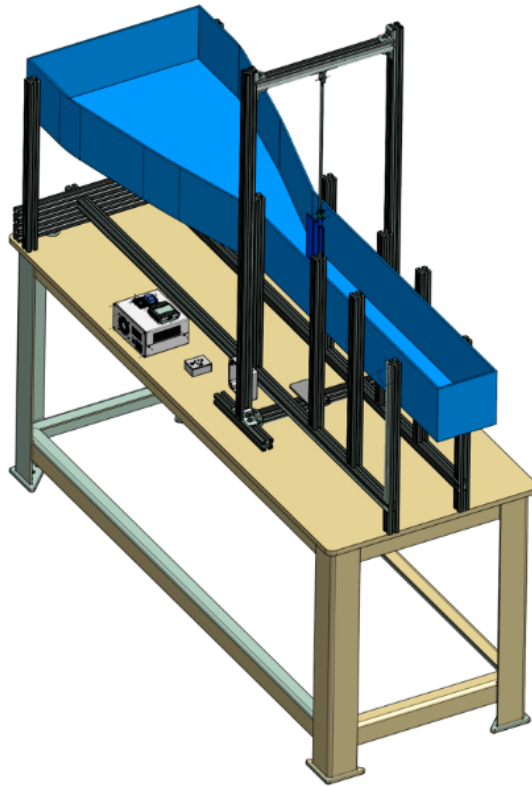


Figure 9. CAD model of the complete experimental setup, including the water channel, t-slots, and structural components for testing the airfoils (zoom-in may be required).

The strain gauges at the top of the cantilever beam were soldered to wires and connected to a Wheatstone bridge powered by a DC power supply. The Wheatstone bridge was also connected to a NI DAQ I/O device that—with the help of a LabView VI—outputted voltages generated by the deflection of the cantilever beam to a desktop device. From there the data was analyzed.

2.5 Procedure

2.5.1 Calibration of the Strain Gauges

The study began by first calibrating the two *Omega SGD-7/350-LY13* precision strain gauges attached to the cantilever beam. The setup for the calibration included a wire pulley system, where a thin plastic wire was attached at the quarter-chord of the airfoil and pulled in tension by 1 g, 3 g, 5 g, and 10 g calibration weights. The strain gauges were soldered to wires that connected to the Wheatstone bridge powered by the DC power supply to convert changes in resistance to a quantifiable displacement. Finally, a NI DAQ I/O device was connected to the Wheatstone bridge and desktop device to get mean voltages for each tension force.

A breakdown of the calibration setup can be seen in **Fig. 10**.

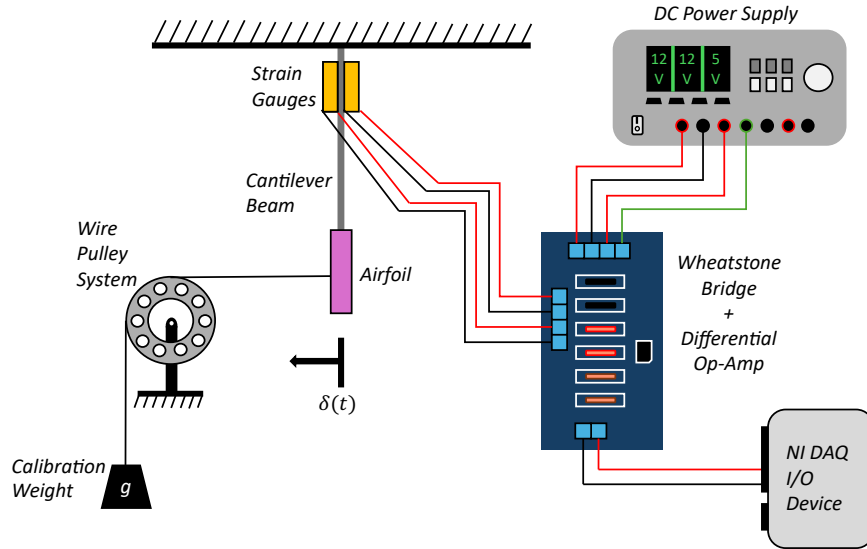


Figure 10. System calibration setup consisting of wire pulley, calibration weights, DC power supply, DAQ, and Wheatstone bridge with differential op-amp. As calibration weight increases, the cantilever beam deflects, and the subsequent voltage change is recorded.

The purpose of the calibration setup was to establish a proportional relationship between strain, voltage, and displacement. With the system calibrated and a sensitivity value achieved, testing in the water channel could begin.

2.5.2 Water Channel Testing

The water channel included a *GS2 Series AC Motor Driver*, and a driver powered a motor of an impeller for the water channel. To ensure a consistent Reynolds number of 4000, the flow speed was set to $4 \pm 0.4 \text{ cm/s}$. For each test trial, the angle of attack was varied from -3° to 17° using the previously discussed AoA connector pieces. The first airfoil tested was the smooth, then the intermediate, then the extreme. For the LabView VI recording voltages from the strain gauges for each trial, a sampling rate of 1000 Hz and 5000 samples were used. Each time trace was then converted into a *.lvm* file and processed inside MATLAB. There was significant noise at higher frequencies than was expected by the observable oscillation of each airfoil. To reduce the noise of the datasets, the time trace data for each airfoil, at each AoA, was processed through a low-pass Butterworth filter. The transfer function of the low-pass filter was found iteratively until a sixth order system with a cutoff frequency of 75 Hz provided sufficient noise reduction, which was an example recommended in the MathWorks documentation [5].

3. Results

3.1 Calibration Results

As previously described in Section 2.5.1, calibration tests were conducted for the *Omega SGD-7/350-LY13* precision strain gauges attached to the cantilever beam. After plotting each case's voltage against their respective tension forces, a linear relationship was recorded between the

two variables. The slope of the calibration curve was used to correlate the voltages recorded by the strain gauges from the deflection of the cantilever beam to a force. The calibration curve from the two Omega SGD-7/350-LY13 precision strain gauges used in this study is seen in **Fig. 11**.

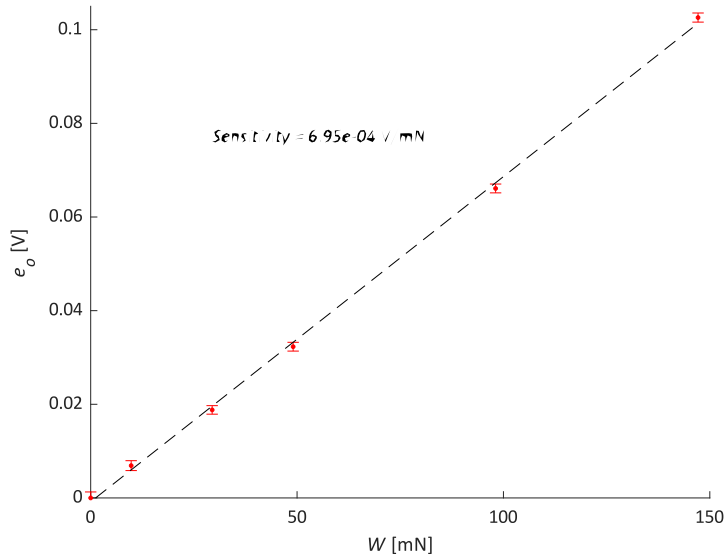


Figure 11. Results of strain gauge calibration testing as shown in Fig. 10 – airfoil loading related to the generated strain gauge voltage.

With the sensitivity of $6.95 \times 10^{-4} V/mN$, voltages from the water channel tests were able to be converted into force in N .

3.2 Lift Coefficient (C_L) vs. Angle of Attack (α)

The experimental setup from Section 2 and with the calibrated strain gauges were implemented for the three airfoils with each of the AoA connector pieces. The aggregated C_L data for all airfoils is shown in **Fig. 12**.

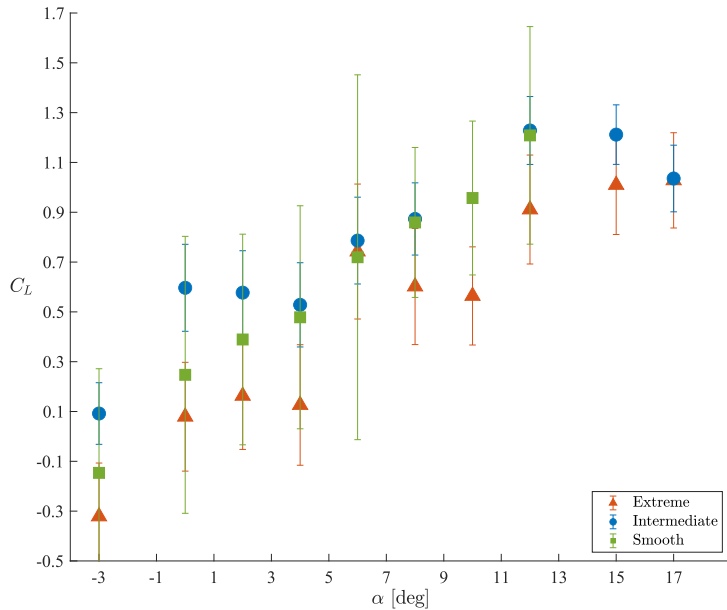


Figure 12. Lift coefficient (C_L) vs angle of attack (α) from experimental strain gauge deflection measurements for smooth, intermediate corrugated, and extreme corrugated airfoils.

3.3 Flow Visualization

In addition to the collected C_L vs α data from the strain gauges, a visual aspect to the tests was created through flow visualization. The flow visualization consisted of injecting blue food coloring dye at the head of the water channel and letting it contact the airfoil. With this, vortices and streamlines were visible and served as validation of the presence of forces recorded by the strain gauges. A snapshot of the flow visualization for all three airfoils at an angle of attack of 0° is shown in **Fig. 13**.

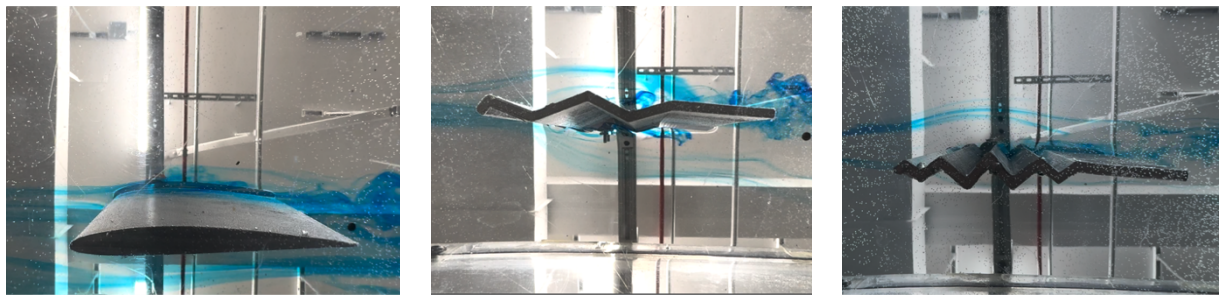


Figure 13. Flow visualization for all airfoils at an angle of attack of 0° . Differences in camera angle may bias observations toward the top surface (coordinates omitted for visual clarity).

Moving from 0° to higher angles of attack, the flow visualization began to demonstrate more pronounced vortex formations and flow separations, particularly for the corrugated airfoils. These differences are highlighted in **Fig. 14**, which captures the results at 3° AoA.

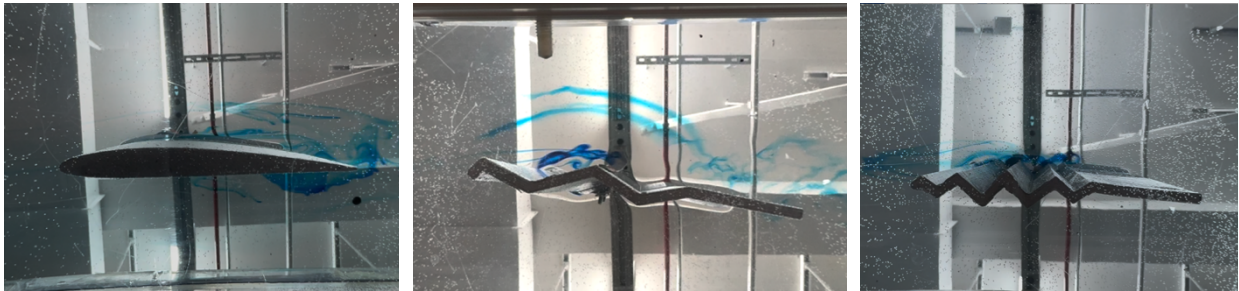


Figure 14. Flow visualization results for all airfoils at an angle of attack of 3° (coordinates omitted for visual clarity).

As the AoA increases to 6° , as shown in **Fig. 15**, the flow behavior changes further, revealing separation zones and recirculation regions.



Figure 15. Flow visualization for all airfoils at an angle of attack of 6° . Extreme airfoil tested in the presence of previous dye to conserve water (coordinates omitted for visual clarity).

Further analysis and interpretation of these observations will be discussed in Section 4.

4. Discussion

4.1 Stall Angle Challenges

One of the primary goals with airfoil testing is to establish a sufficient range of angles of attack to capture the stall angle. Although the research by Tang al. went up to an AoA of 12° , this experiment aimed to expand that range by adding a 5° buffer, testing all the way up to an AoA of 17° . Upon testing, the intermediate airfoil, the region of 12° to 15° was determined to contain the stall angle due to the mean C_L being maximized at $C_{L,intermediate} = 1.2 \pm 0.1$.

Additionally, **Fig. 16** demonstrates flow separation furthermore proving that $\alpha = 12^\circ$ approaches the stall angle.



Figure 16. Flow visualization for the intermediate airfoil at $\alpha = 12^\circ$ using a higher zoom level to highlight flow separation and vortex formation indicative of stall conditions (coordinates omitted for visual clarity).

As can be seen in **Fig. 16**, the flowing vortices appear to diverge from the upper surface of the airfoil as they approach approximately half the chord length. This is an indicator of a growing boundary layer separation. As was stated earlier, this is corroborated with the intermediate data in **Fig. 12** as approaching stall. The data for the upper angles of attack for the extreme and the smooth airfoils were met with more uncertainty and led to a failure of the experimental data collection, as seen in **Fig. 12**. The strain gauge voltages had oscillated to the point at which no steady-state deflection could be reached for a useable set of data. Due to this, the characteristic dip in C_L could not be determined for these airfoils.

4.2 Performance Comparison of the Airfoil Designs

The most apparent analysis that can be drawn from the aggregated data in **Fig. 12** is that no *definitive* statement of the performance of one airfoil versus the other can be made due to the overlapping uncertainty bounds. The following discussion is therefore a statement on what could be suggested by the mean values of the data as an impetus for more precise studies. When analyzing the aerodynamic lift data for the three airfoils in **Fig. 12**, it is evident that the mean values for the extreme corrugation airfoil performed worse than the smooth and intermediate corrugations. For angles of attack between -3° and 17° , C_L for the extreme corrugation airfoil was consistently the lowest of the three airfoil test cases. For example, at $\alpha = -3^\circ$, $C_{L,smooth} = -0.1 \pm 0.4$, $C_{L,intermediate} = 0.1 \pm 0.1$, and $C_{L,extreme} = -0.3 \pm 0.2$. This is highly suggestive evidence that the extreme corrugation airfoil was not producing increased lift as to suggest a substantial improvement in airfoil design from this experimental concept.

In contrast, the intermediate corrugation airfoil's mean values were suggestive of a possible improvement. The mean values of **Fig. 12** suggests that there is a lift advantage to using the intermediate airfoil for angles of attack between -3° and 6° . While still in the range of uncertainty, the fact that the biggest difference in mean C_L was found in the region between 0° and 6° shows a promising similarity to the phenomenon captured by Tang et al [4]. Conversely, the mean C_L data at higher angles of attack yields no distinct trend. Starting at $\alpha = 7^\circ$, mean

values begin to overlap as the intermediate corrugation airfoil behaves similarly to the smooth airfoil. At $\alpha = 12^\circ$, $C_{L,smooth} = 1.2 \pm 0.4$, $C_{L,intermediate} = 1.2 \pm 0.1$, and $C_{L,extreme} = 0.9 \pm 0.2$. The mean C_L value for the extreme corrugation airfoil is still the lowest of the three, but the difference between the mean C_L value for the intermediate and smooth airfoil is nonexistent.

These results, while ultimately inconclusive due to the uncertainty, do establish a reason to continue testing with slight modifications and a change in the scale of the experimental setup. Future experimentation would revolve around the intermediate and smooth airfoils, while eliminating the extreme corrugation airfoil as the flow do to the data in **Fig. 12**. This is consistent with the fact that, visually, the flow seems to be perturbed and separated by the steep slopes of the compressed corrugation sections. Though a qualitative measure, there are no instances of vorticity present in the corrugations of the extreme (in **Fig. 13-15**) as were captured in the intermediate (in **Fig. 13-15**). Although, PIV would be needed to definitively show whether the low-pressure flow reaches the more aft ward corrugations, so it would be worth including for any immediate PIV extensions of this experiment. The primary goal for future testing would be to identify and minimize as many sources of uncertainty as possible.

4.3 Sources of Uncertainty

One of the primary sources of uncertainty was the potentiometer used for controlling the water speed in the water channel. During testing, the input frequency used to control the speed would fluctuate and thus cause the airfoil to vibrate instead of staying still. This slight vibration resulted in relatively large uncertainty bars seen in **Fig. 12**. This problem did make sense as there was oxidation discovered on the printed circuit board (PCB) right around the potentiometer. Upon de-soldering, cleaning, and re-soldering, the magnitude of the fluctuation decreased, but it still existed.

Another source of uncertainty was from the blockage effects of the airfoil at higher angles of attack. Given that the testing section of the water channel had a cross-sectional area 170 cm^2 and the wings had a chord length of 10 cm , there is reason to suspect that blockage effects were present. This reduced flow speed combined with a faulty potentiometer significantly hindered the reliability of the entire testing setup, thus leading to high uncertainties. This furthermore impeded the ability of the lift values to representative of an “infinite” 2D wing.

Similarly to blockage, there were also wing-tip effects present in the system due to the nature of the setup. Since the system is assumed to be 2D with the airfoil being fully submerged underwater, the fact that there was space between the bottom of the water channel and the airfoils created wing-tip effects. The wingtip and blockage effects added more uncertainty to the lift calculations in terms of a direct comparison with the Tang et al numerical study. It is for this reason that this study does not compare the literature and experimental datasets directly. It instead tried to find the same superior lift relationship of corrugated airfoils against a conventional airfoil as the control– as declared by the conclusions of Tang et al. [4].

Finally, another source of uncertainty was the physical stability of the experimental setup. Given that the entire water channel was powered by a motor driving an impeller, there was a notable amount of vibration and friction present in the system. Although the testing frame was

constructed out of aluminum and was visibly stable, it was still susceptible to outside vibrations. These vibrations hindered the reliability of deflection data collection.

4.4 Capturing the Vorticity

A key objective of this experiment was to capture the vorticity of the flow in the corrugations of the airfoil. The following flow visualization from **Fig. 14** is emphasized as **Fig. 17** for further discussion.

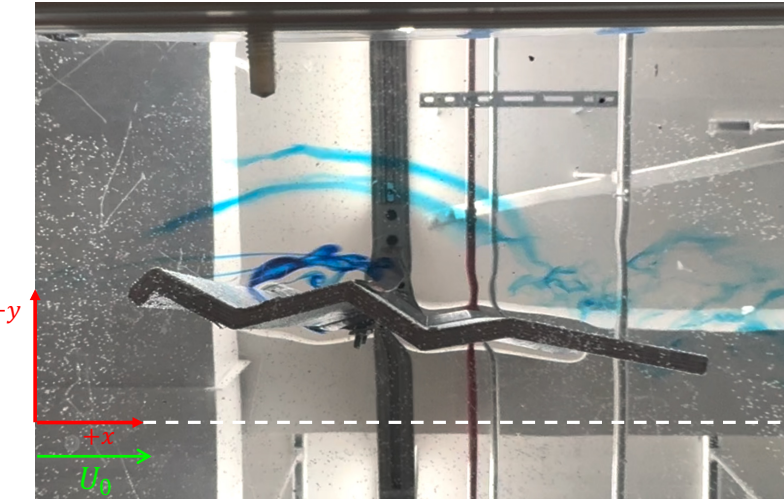


Figure 17. Flow visualization of the intermediate airfoil at $\alpha = 12^\circ$, showing flow separation and stall onset.

Aside from the numerical lift data, the flow visualization was one of the major successes of this experiment. Tang's research suggested that vortices would form in between the corrugations on the airfoils, which would theoretically reduce pressure and increase lift [4]. As seen in **Fig. 17**, the flow visualization for the intermediate airfoil clearly demonstrates vortices forming in-between the corrugations, thus potentially reducing pressure and increasing lift. This trend persisted across varying angles of attack, furthermore, solidifying the vorticity hypothesis.

As for the extreme corrugation airfoil flow visualization from **Fig. 15**, the space in between the corrugations was not large enough for any vortices to form, thus potentially resulting in a lower lift coefficient across all angles of attack. However, with a different flow speed and subsequently a different Reynolds number, the extreme corrugations may have vortices form in-between them. However, given the testing circumstances of this experiment, altering the Reynolds number for the extreme corrugation airfoil would have to be delegated to potential future testing.

4.5 Project Cost Breakdown

A detailed cost breakdown of all the components used in this study can be seen in **Appendix A**. Initially it was planned that load cells and force sensors would be used for force measurements. Given that there were no waterproof load cells and force sensors readily available and they each cost hundreds of dollars, the idea to measure deflection from a cantilever beam to quantify forces was chosen to minimize costs.

In addition to using a cantilever beam deflection to measure aerodynamic forces, the water channel was chosen as the testing system. Originally, it was planned for the wind tunnel to be used. Given that the Reynolds number of 4000 would have forces on the $< 1 \text{ mN}$ scale, a decision was made to switch to the water channel due to the higher density of the fluid. This was also part of minimizing costs as operating the water channel was cheaper than operating the wind tunnel.

Although the study adhered to the \$400 budget for new materials, the overall project incurred costs exceeding \$30,000. Most of these expenses were operational costs for resources like the water channel, 3D printing, and machining, which were covered by the AME department at the University of Southern California. These resources were pre-existing and not purchased specifically for this study. Additionally, software licenses for SolidWorks and Siemens NX were provided by USC, further reducing additional costs.

In retrospect, the cantilever beam and strain gauge setup could have been designed better initially. The issue lied in attaching the strain gauges properly to the beam without the wires on each of the strain gauges contacting the beam. In addition, the first set of strain gauges took on a voltage that exceeded their operational limits and overloaded. As a result, if the initial design was to glue the strain gauges to the beam and solder them to wires, some expenses could have been saved.

5. Conclusion

5.1 Summary

This experiment was ultimately a success, but not in a traditional manner. Rather than proving the hypothesis that corrugated airfoils provide more lift than non-corrugated airfoils, the results provided a reasonable foundation for future testing with more sophisticated equipment. While the extreme corrugation airfoil mean C_L values performed consistently worse than the smooth control airfoil, the intermediate corrugation airfoil did show the beginnings of an aerodynamic advantage trend. As demonstrated in **Fig. 12**, the mean C_L values for the intermediate corrugation airfoil were on average 27% larger than the smooth airfoil for angles of attack between 0° and 6° . These findings alongside the research by Tang et al. suggest that there may be legitimate aerodynamic advantages to using corrugated airfoils as opposed to non-corrugated airfoils [4]. However, it's important to note that there does seem to exist a limit as to how corrugated the airfoil can be before it drops off in aerodynamic performance.

5.2 Recommendations

The primary recommendation for future testing revolves around a refurbishment of the water channel. As mentioned in Section 4.3, the potentiometer used for controlling water speed was malfunctioning which led to high uncertainty in the lift calculations. In addition to that, future testing should be conducted in a larger water channel to minimize blockage effects at higher angles of attack. With a larger working water channel, C_L uncertainty would be significantly smaller leading to more precise data.

Another recommendation for future testing would be to use a heavier and sturdier frame for holding the airfoil. Since the motor providing power to the water channel causes noticeable vibrations in the setup, a tougher frame would minimize those vibrations and subsequently leads to more stable data. In addition to that, a supplementary method for deflection data collection should be implemented into the setup. For example, a high-precision laser displacement sensor (such as a *Keyence LK-G402*) would notably reduce uncertainty in the deflection measurements for the cantilever beam.

The final recommendation for future testing is to utilize particle image velocimetry (PIV) to properly analyze the flow, vortices, and streamlines over the airfoils. Although not entirely necessary, PIV would greatly aid in better understanding the numerical results behind each of the tested airfoils.

6. References

- [1] J. D. Anderson, *Introduction to Flight*, 9th ed. New York, NY, USA: McGraw-Hill Education, 2022.
- [2] T. Deubel, S. Wanke, C. Weber, and F. Wedekind, 'Modelling and Manufacturing of a Dragonfly Wing as Basis for Bionic Research', *Strojarstvo*, vol. 49, 01 2008.
- [3] NASA, "NACA airfoils," NASA, 2015. [Online]. Available: <https://www.nasa.gov/image-article/naca-airfoils/>
- [4] H. Tang, Y. Lei, X. Li, and Y. Fu, 'Numerical Investigation of the Aerodynamic Characteristics and Attitude Stability of a Bio-Inspired Corrugated Airfoil for MAV or UAV Applications', *Energies*, vol. 12, p. 4021, 10 2019.
- [5] MathWorks, "Butterworth filter design," MATLAB Signal Processing Toolbox, 2024. [Online]. Available: <https://www.mathworks.com/help/signal/ref/butter.html>

7. Appendices

7.1 Appendix A: Budget Analysis

AME-441 Group 24 - Cost Estimate Experimental Analysis of Dragonfly-Inspired Airfoils at a Reynolds Number of 4000 as of 12/11/24					
	Vendor/Manufacturer	Model/Part No.	Qty.	Unit Price	Item Price
EXPENSES FOR ITEMS AVAILABLE IN LAB					
Equipment					
USB Multifunction DAQ	National Instruments	USB-6211	1	\$792.00	\$792.00
Water Channel Testing (\$350 per hour)	USC	N/A	60	\$350.00	\$21,000.00
Strain Gauges	AME-441 Lab	Omega SGD-6/120-LY41	2	\$77.13	\$154.26
Rigol DP832 Multichannel Power Supply	AME-441 Lab	DP832	1	\$473.00	\$473.00
Services					
SOLIDWORKS	USC Software License	N/A	1	\$2,620	\$2,620
Siemens NX	USC Software License	N/A	1	\$1,395	\$1,395
NI LabVIEW	USC Software License	N/A	1	\$528	\$528
MATLAB	USC Software License	N/A	1	\$275	\$275
Materials					
ABS Filament (Spool)	AME-441 Lab	N/A	10	\$20.00	\$200.00
Sandpaper	AME-441 Lab	N/A	1	\$14.99	\$14.99
1.5" x 1.5" Hollow T-Slots	AME-441 Lab	47065T101	6	\$32.13	\$128.52
1.5" x 1.5" Corner Brackets	AME-441 Lab	47065T845	14	\$8.80	\$123.20
1" Extended Corner Bracket	AME-441 Lab	1556A61	2	\$8.00	\$16
18-8 Stainless Steel Button Head Hex Drive Screws	AME-441 Lab	92620A535	1	\$5.57	\$5.57
10-32 x 3/4 Flathead Screw	AME-441 Lab	91253A008	1	\$15.88	\$15.88
Steel Offset-Barrel Narrow-Base Weld Nuts	AME-441 Lab	93560A230	1	\$11.14	\$11
M2 x 0.4 mm Fully Threaded Screw	AME-441 Lab	92095A455	1	\$7.88	\$8
Single Nut with Center Hole	AME-441 Lab	90870A113	1	\$3.30	\$3
Size #10 Hex Nuts	AME-441 Lab	95462A525	1	\$12.17	\$12
Manufacturing					
3D Printing (\$40 per hour)	AME-441 Machine Shop	Prusa XL 3D Printer	50	\$40.00	\$2,000.00
Machining (\$40 per hour)	AME-441 Machine Shop	N/A	6	\$40.00	\$240.00
					Sub-total Cost: \$30,015.91
EXPENSES FOR ITEMS REQUIRED FOR PURCHASE					
Materials					
Food Coloring Dye for Flow Visualization (<i>In progress</i>)	Amazon	B0080GD2RK	5	\$12.00	\$60.00
Phone Tripod	Amazon	B08SBQN81V	1	\$25.95	\$25.95
Pulley system	Amazon	N/A	1	\$10.21	\$10.21
Calibration Weights	Amazon	B09ZYC6HNZ	1	\$9.99	\$9.99
Aluminum 6061 0.04" thick sheet, 2" x 24"	McMaster	89015K161	3	\$5.56	\$16.68
1" x 1" Hollow T-Slot (5 Feet)	McMaster	47065T101	1	\$43.06	\$43.06
1" x 1" Corner Brackets	McMaster	47065T236	8	\$7.92	\$63.36
Aluminum 6061 0.04" thick sheet, 2" x 24"	McMaster	89015K161	2	\$5.56	\$11.12
					Sub-total Cost: \$240.37
					TOTAL PROJECT EXPENSES: \$30,245.16
BUDGET					
AME-441 project budget (\$100 per student)			4	\$100.00	\$400.00
					TOTAL BUDGET: \$400.00

Figure 18. Detailed Cost Estimate for Group 24.

Table 1. Breakdown of project costs, including estimated expenses for equipment, materials, and resources provided by the USC lab.

Category	Cost Estimate (USD)	Notes
Water Channel Usage	\$21,000	60 hours of usage, provided by USC lab.
3D Printing and Machining	\$2,240	50 hours 3D printing, 6 hours machining at \$40/hour.
Software Licenses (SolidWorks, Siemens NX, MATLAB)	\$4,818	Provided by AME department.
Purchased Materials (e.g., Aluminum Sheets, Dye)	\$240	Materials purchased specifically for the project.
Miscellaneous Costs	Included in Lab Resources	Other resources already available in Biegler Hall lab.

7.2 Appendix B: Engineering CAD Drawings

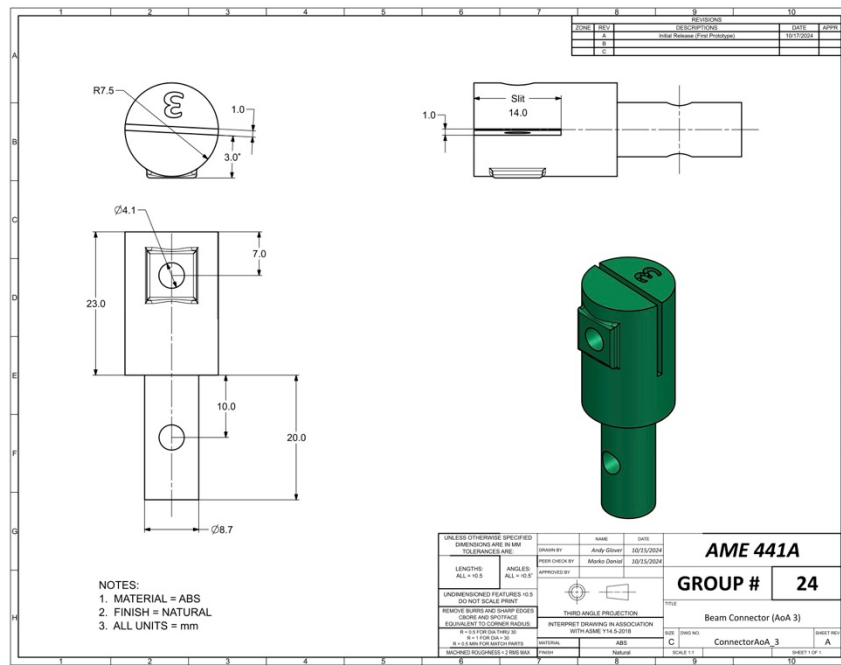


Figure 19. Engineering drawing of AoA connector piece (at AoA = 3°), showing design changes for improved stability at various angles of attack.

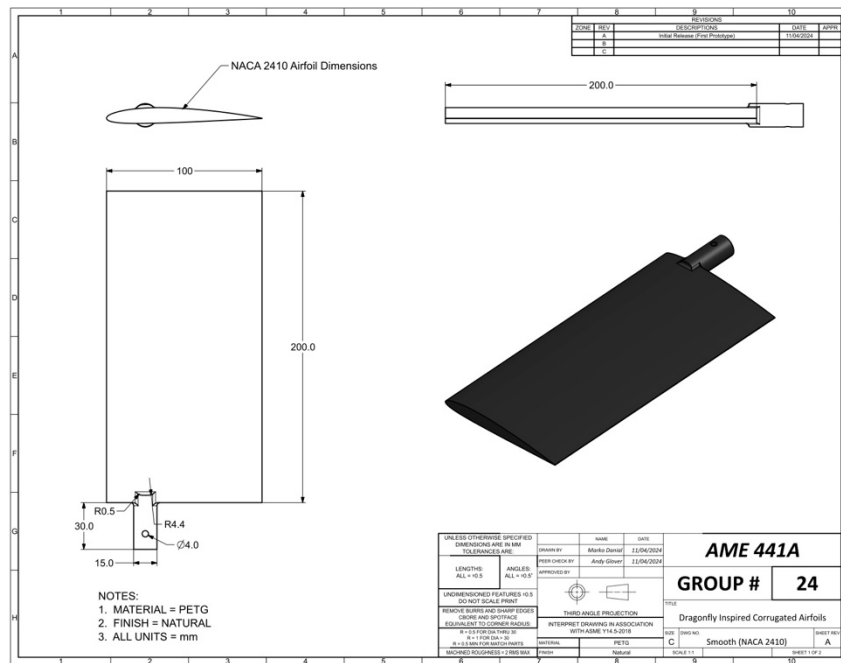


Figure 20. Engineering drawing of the NACA 2410 smooth airfoil for aerodynamic efficiency analysis.

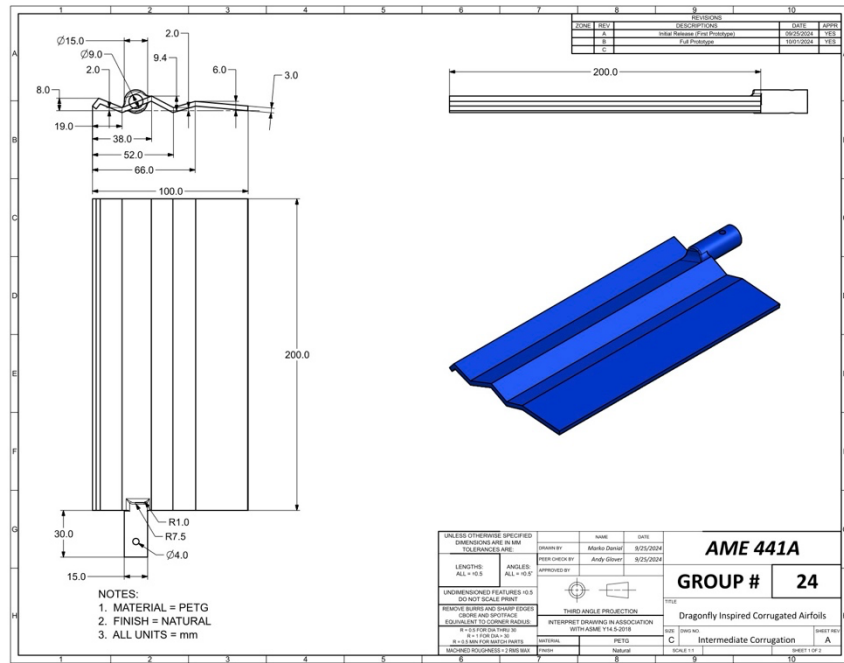


Figure 21. Engineering drawing of the intermediate corrugated airfoil for aerodynamic efficiency analysis.

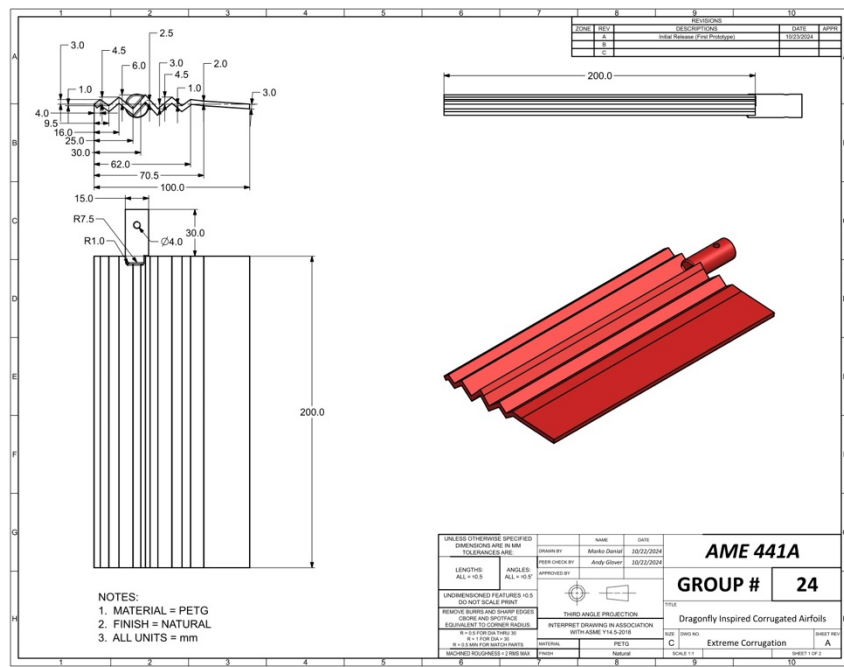


Figure 22. Engineering drawing of the extreme corrugated airfoil for aerodynamic efficiency analysis.

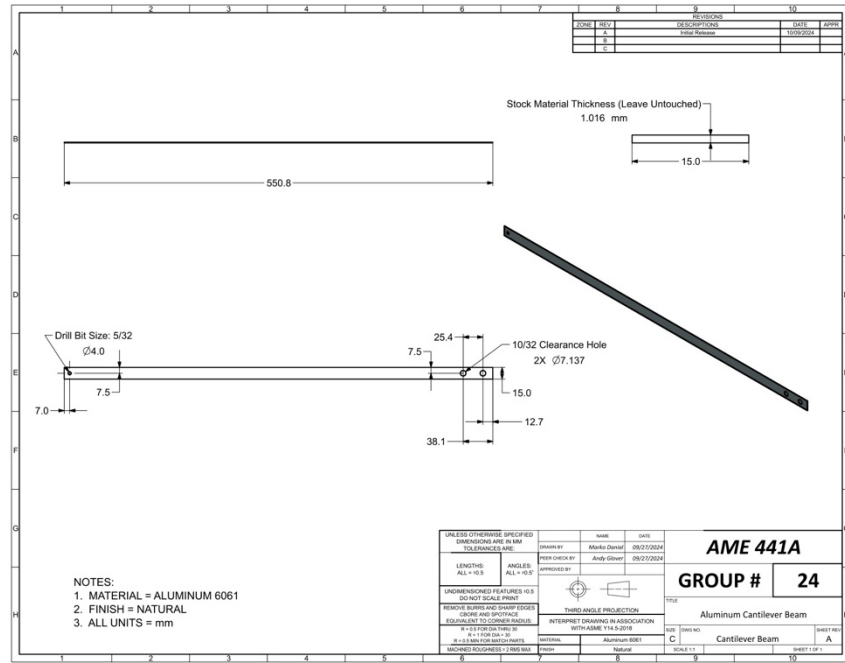


Figure 23. Updated engineering drawing of the Aluminum 6061 cantilever beam for stability and precision.

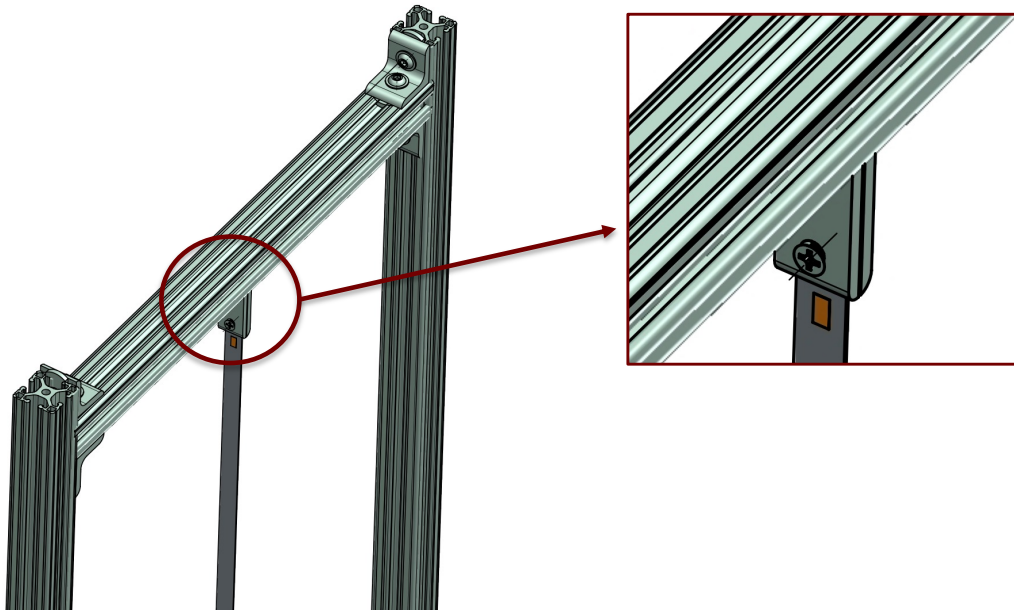


Figure 24. Close up to show beam fixture, airfoil fixture, and strain gauge integration.

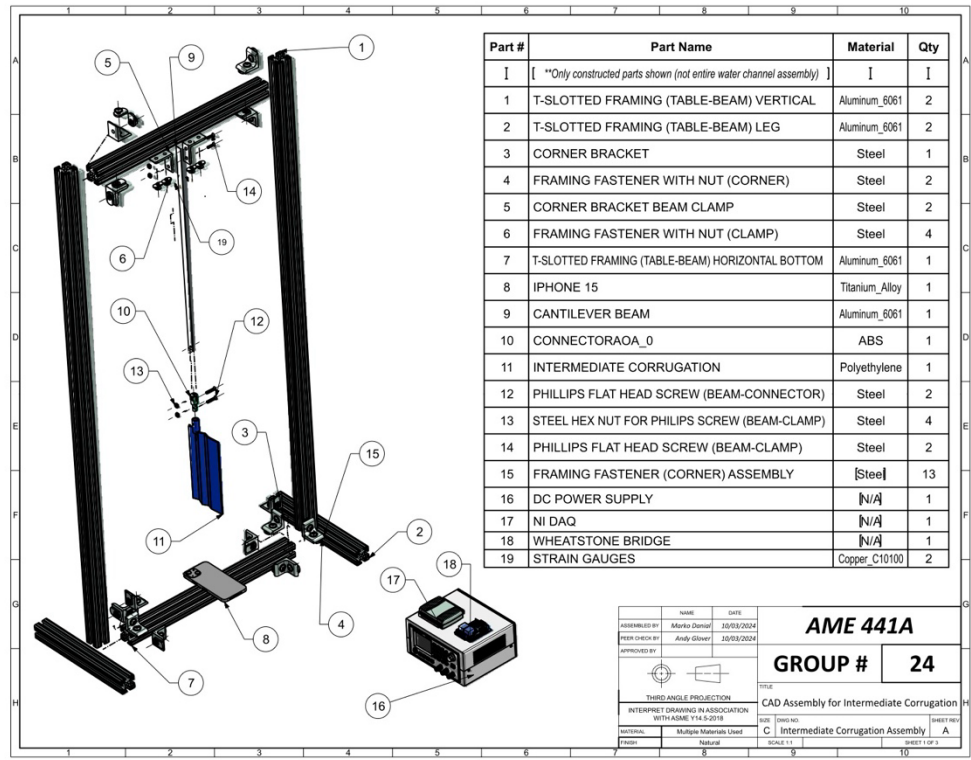


Figure 25. Exploded view CAD drawing of the cantilever beam stand and t-slot supports, along with a Bill of Materials (BOM) listing all components, materials, and quantities required for the experimental setup.